Article

Tensile Properties of Ex-Situ Ti-TiC Metal Matrix Composites Manufactured by Laser Powder Bed Fusion

Gaëtan Bernard * , Vaclav Pejchal , Olha Sereda , Roland E. Logé

Posted Date: 14 October 2024

doi: 10.20944/preprints202408.0490.v2

Keywords: metal matrix composite; titanium alloy; titanium carbide; additive manufacturing; mechanical properties; microstructural properties

Preprints.org (www.preprints.org) | NOT PEER-REVIEWED | Posted: 14 October 2024 doi:10.20944/preprints202408.0490.v2

Article

Tensile Properties of Ex-Situ Ti-TiC Metal Matrix Composites Manufactured by Laser Powder Bed Fusion

Gaëtan Bernard [1,2,*], Vaclav Pejchal [1], Olha Sereda [3] and Roland E. Logé [2]

[1] Additive Manufacturing and Component Reliability Group, CSEM SA, Rue Jaquet-Droz 1, Neuchâtel CH-2002, Switzerland
[2] Thermomechanical Metallurgy Laboratory, PX Group Chair, Ecole Polytechnique Fédérale de Lausanne (EPFL), CH-2002 Neuchâtel, Switzerland
[3] Etat de Neuchâtel, Rue de la Collégiale, CH-2002 Neuchâtel, Switzerland
* Correspondence: gaetan.bernard@csem.ch

Abstract: Titanium-based Metal Matrix Composites (MMCs) manufactured by additive manufacturing offer tremendous lightweighting opportunities. However, processing the high reinforcement contents needed to substantially improve elastic modulus while conserving significant ductility remains a challenge. Ti-TiC MMCs fabricated in this study report fracture strains in tension up to 1.7% for a Young's modulus of 149 GPa. This fracture strain is 30% higher than previously reported values for Ti-based MMCs produced by Laser Powder Bed Fusion (LPBF) displaying similar Young's moduli. The heat treatment used after the LPBF process leads to the doubling of the fracture strain due to the conversion of TiC_x dendrites into equiaxed TiC_x grains. As-built microstructure shows both un-dissolved TiC particles and sub-stoichiometric TiC dendrites resulting from a partial dissolution of TiC particles. Reduction of the C/Ti ratio in TiC during the process results in an increase in the reinforcement content, from a nominal 12 vol% to an effective 21.5 vol%. The variation of the TiC lattice constant with its stoichiometry is measured, and an empirical expression is proposed for its effect on TiC's Young's modulus. The lower TiC initial powder size distribution displayed the best mechanical performance.

Keywords: metal matrix composite; titanium alloy; titanium carbide; additive manufacturing; mechanical properties; microstructural properties

1. Introduction

Laser Powder Bed Fusion (LPBF), since its introduction, played a significant role in refining Titanium alloys exceptional properties in terms of ductility, stability at high temperature, specific strength along with resistance to corrosion. Standing out within the metal Additive Manufacturing (AM) landscape, the LPBF method offers a greater degree of flexibility in terms of shapes, as well as potential to reduce the total number of components of a part compared to traditional metallurgical processes. Moreover, this technology is particularly suited for medical and aerospace applications, as it implies high cooling rates which then induce a strongly refined microstructure.

Further mechanical properties enhancement can, however, be obtained by reinforcing Ti alloys with a second component, usually ceramic, and produce a Metal Matrix Composite (MMC). These materials are promising candidates to increase and control specific stiffness. Titanium MMC have been produced by conventional methods and demonstrated remarkable mechanical properties [1]. As an example, Self-propagating High-temperature Synthesis (SHS) and Spark Plasma Sintering (SPS) were used by Lagos et al. to produce Ti64-TiC MMC with a Young's modulus improvement of 15%, while keeping the fracture strain above 3% [2]. However, due to the hardness difference between the matrix and the reinforcement, MMCs are usually difficult to machine, and confined to simple shapes. In addition, the hard phase causes a high tool wear rate leading to high machining costs.

Therefore, AM triggers a radical change for MMCs manufacturing, with its ability to produce neat net-shapes, as demonstrated by the number of publications in the field, in the last 15 years.

Several reviews covering the recent advances in the use of LPBF to fabricate Ti-based MMCs were published in the last years [3–5] and give insights into the researcher's focus points. Firstly, the main reinforcements for Ti-based MMCs are TiC and TiB and can be introduced directly as TiC and TiB2 or by using C and B precursors which will react with Ti to form carbides and borides. Secondly, a majority of the studies focus on strength and wear resistance enhancements which require lower reinforcement contents than elastic modulus enhancement. Thirdly, producing a significantly strengthened MMC displaying a significant elongation is still challenging. This is reflected by the minority of studies reporting elongation values. For example, Xi et al. worked on Ti reinforced by 30 vol% of TiC, TiN, a mix of both, as well as graphene [6]. They could produce parts with each type of powder mix but could not produce crack-free Ti-TiC and Ti-TiN samples. Moreover, they also studied the hardness of the achieved MMCs and showed that TiC produces the highest strengthening effect. Radhakrishnan et al. alternatively demonstrated the possibility of producing crack-free Ti-TiC coatings with up to 20 vol% reinforcement content by LMD, which opens the possibility of reaching this reinforcement content in bulk components [7]. Gu et al. demonstrated a very promising stiffness increase, from nanoindentation tests, in LPBF produced Ti reinforced by 15 wt% TiC nanoparticles which displayed a nano-hardness of 90.9 GPa with a local reduced modulus of 256 GPa [8,9]. While there is no indication of the ductility of the produced MMC, it does however display the potential of such reinforcement content. Yan et al. reinforced Ti6Al4V with graphene by LPBF and, despite the low 0.5 wt% of reinforcement content, could achieve a strong strengthening effect with an Ultimate Tensile Strength (UTS) of 1526 MPa and Young’s modulus of 145 GPa [10]. The reported fracture was, however, only 1.3%. Additionally, using the identical powder mix and reinforcement content, the same study compared these results with parts produced with SPS for which the strengthening effect was much lower. As demonstrated by the latter displaying an UTS of 877 MPa, a Young’s modulus of 115 GPa and the fracture strain increased to 3.9%. They assumed that the discrepancy was due to graphene reacting at elevated temperature with Ti to form TiC, and proposed that the short process time scale in LPBF prohibited the reaction to occur. This study demonstrates, to the authors knowledge, the highest fracture strain in tension for Ti-based MMCs produced by LPBF displaying significant stiffness improvement (with 1.3% fracture strain for an elastic modulus of 145 GPa) [10]. Ti-based MMCs produced by conventional methods have been reported as early as the 2000s to achieve elongation of 2.5 to 3% for such elastic moduli which demonstrates the need for further research on the subject [1].

TiC in Ti-TiC MMCs is known for its deviation from the equilibrium phase diagram in terms of C/Ti ratio. The groups of Andrieux et al. as well as Roger et al. studied the evolution of this ratio in Ti-TiC MMCs during heat treatment and observed an experimentally stable C/Ti ratio of 0.57 in the TiC phase [11,12]. Lin et al. demonstrated an inverse relation between the cooling rate and the obtained C/Ti ratio [13]. The variation of the C/Ti ratio affects the effective reinforcement content through the distribution of the C atoms over a larger number of TiC molecule but also a variation of the lattice constant. Moreover, mechanical properties are also impacted by this variation. Kurlov and Gusev compiled the available data and proposed empirical relations for the lattice constant, shear modulus and Poisson ratio as a function of the C/Ti ratio [14]. It is, hence, recommended to study the evolution of the reinforcement from the powder stage (nominal volume fraction) to the finished MMC (effective volume fraction) which is often neglected in mechanical properties related studies. Referring only to the nominal content of reinforcement may significantly underestimate the volume fraction, depending on the achieved stoichiometry.

The investigation aims at improving the fracture strain in tension of a Ti-TiC MMC displaying a significantly enhanced Young’s modulus . It uses a 3-steps process consisting in mechanical blending, LPBF process and heat treatment, as well as investigates several size distributions of TiC powders to determine the optimal one for stiffness-driven Ti-TiC MMCs. In order to ensure practicality and scalability of the process, we focus readily available and easily producible forms of TiC: comminuted

TiC powders. For the same reason, the mechanical properties are characterized by tensile testing on near-net-shape ASTM E8M compliant tensile samples [15].

2. Materials and Methods

The full metal-matrix composite manufacturing process is explained in detail in the next sections and summarized in Figure 1. It consists in a powder preparation step in which a premix is prepared mechanically, followed by the LPBF process used to consolidate the MMC. The dendritic TiC microstructure is, then, globularise through heat treatment leading a stabilized microstructure.

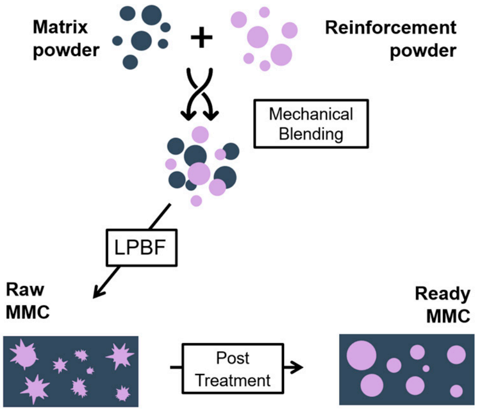

Figure 1. MMC Manufacturing process.

2.1. Powder Preparation

The powder mixture included plasma atomized spherical commercially pure Titanium (Cp-Ti grade 2, 5-45 µm, Figure 2 a) from AP&C, and comminuted 99% purity Titanium Carbide powder (TiC, 5-45 µm, Figure 2 b) from Höganäs GmbH. The comminuted TiC powder was sieved in two different ways, producing two size distributions: One with an upper threshold of 45 µm, the other with a threshold of 23 µm. The first sieving removed all agglomerates from transport and led to the full 5-45 µm distribution. The second one effectively removed all particles larger than 23 µm. Two Cp-Ti/TiC powder blends containing 13 wt% of TiC were prepared by means of a 3D shaker mixer from WAB Group (Turbula T2F) for at least 3h. This blending method uses a motion in three dimensions of the powder container to gently mix the powders and avoid particles damaging. The powder blend using comminuted TiC sieved below 45 µm, and below 23 µm, are referred to as TiC45 and TiC23, respectively. The homogeneity of the distribution of the TiC in the powder blends were visually assessed from several micrographs. One representative micrograph can be found in the Appendix A, Figure A1. The flowability of the raw powders and powder blends were characterized using a GranuDrum™ from GranuTools. The powders flowability were tested over a wide range of rotation speeds. The flowability data were used to select an initial recoating speed for the LPBF process. Additionally, the powder layer absorptivity was measured for pure powders and powder blends, using a Spectrometer from Perkin Elmer (Lambda 950PE) equipped with an integration sphere.

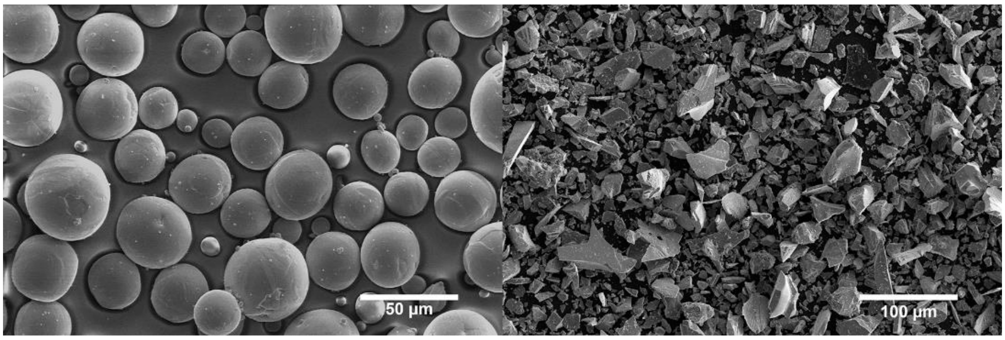

Figure 2. SEM micrographs presenting a) Plasma atomised spherical Titanium powder. b) Comminuted Titanium Carbide Powder.

2.2. Laser Powder Bed Fusion Processing and Heat Treatment

The LPBF process was performed using a commercial machine (TruPrint 1000) from Trumpf GmbH, which was equipped with a 200 W fiber laser with a 30 µm laser spot size. The process was done argon atmosphere with Oxygen concentration limit of 100 ppm. Tensile specimens were prepared on a Ti64 substrate with the optimized laser parameters presented in Table 1 with the Volume Energy Density: $VED = P/Vht$, where laser power is P [W], the scanning speed is V [mm/s], the hatching distance is h [mm], and the layer thickness is t [mm]. A lower energy was used for the sample's contour than for the hatching in the inner region (referred to as "hatching region" from this point) to reduce surface roughness. The laser scanning strategy was bi-directional with 67° rotation from one layer to another. The samples geometry followed the ASTM E8M standard (details are available in the Appendix A, Figure A2 and Table A1) [15]. The samples were printed with their axis parallel to the building direction and by batch of 24.

Table 1. Laser parameters used in LPBF processing. Contour distance refers to the minimum distance between a laser pass from the contour and the hatching region. Contour number accounts for the thickness of the contour in terms of number of laser passes. .

Hatching region		**Contour**	**General parameters**		
VED [J/mm3]	Hatching distance [µm]	VED [J/mm3]	Layer thickness [µm]	Contour distance [µm]	Contour number [–]
166.7	40	52	30	30	1

Samples were encapsulated in quartz tube under Argon atmosphere to avoid oxidation and nitridation and heat treated at 880°C in a furnace from Nabertherm. The heating and cooling rates were set 600 °C/h and all samples were treated simultaneously. Four samples from each set were heat-treated for 24h to globularise TiC dendrites.

2.3. Microstructural and Mechanical Characterization

Samples were cut both along and across the building direction, then ground using SiC paper, and subsequently polished using several grades of diamond paste, and lastly, finished by OP-S solution (Struers). Low-magnification and high-magnification microstructural analysis was done by Scanning Electron Microscopy (SEM, FEI Scios 2 and ZEISS Merlin) using Secondary (SE), Backscattered Electron (BSE) imaging, as well as Electron Backscatter Diffraction (EBSD, Oxford Instruments). General SEM used an acceleration voltage of 10 kV, while EBSD used a 25 kV acceleration voltage. The porosity of the sample was determined first by analyzing low-magnification SE micrographs and, second, by X-ray Computed Tomography (XCT, Phoenix V|tome|x M from Weigate Technologies). Image analysis considered a minimum of five micrographs per sample and used an in-house developed Python script. The TiC reinforcement content was determined using the same image analysis method, from low-magnification micrographs when un-dissolved, and high-magnification micrographs when dendritic and granular. Etching provided by the OP-S solution sufficed to clearly distinguish the Ti grains. Phase composition was characterized by X-Ray Diffraction (XRD, PANalytical X'Pert PRO with PIXcel source at 45 kV and 40 mA). The variation of the C content in heat-treated TiC grains was evaluated by Scanning Transmission Electron Microscopy (STEM, Titan Themis, Thermo Fischer) and Energy Dispersive X-Ray Spectroscopy (EDS) with an acceleration voltage of 200 kV. TEM lamellas were prepared in a SEM by Focused Ion Beam (FIB, FEI Scios 2).

Tensile properties were characterized on as-built and heat-treated tensile samples at room temperature employing a 100kN tensile machine (Zwick Serie E) according to the ASTM 8M/E8M standard, using a strain rate of $8.33 \cdot 10^{-5}\ s^{-1}$ [15]. The measurement of the strain during the test was done by three means: with a Digital Image Correlation (DIC) system from GOM focused on one side of the sample, with a strain gage glued on the other side of the sample, and with a clip-on extensometer. The machine strain rate was controlled using the clip-on extensometer. The tensile test was interrupted at 300 MPa and 700 MPa and unloaded to 100 MPa, producing two unload/reload cycles. These allowed measuring the Young's modulus and overall elastic response of the sample. Data from at least 4 samples were averaged for each analysis. Finally, the fracture surfaces and cross-sections beneath them were observed by SEM to characterize failure mechanisms.

3. Results and Discussion

3.1. As-Built MMCs Microstructure

The microstructures of TiC23 and TiC45 in as-built conditions were studied by SEM. Figure 3 shows typical BSE micrographs of TiC23 (top) and TiC45 (bottom). It displays a light grey Ti-matrix hosting a homogeneous distribution of dark grey TiC dendrites (see arrows: yellow B and green C) as well as black un-dissolved TiC particles (red arrow A). Similar microstructures were observed by Gu et al. for similar TiC content in the powder mix [8]. Dendritic TiC is present in two subsets: (i) primary TiC precipitating from the liquid (yellow arrow B), and (ii) secondary TiC originating from the diffusion layer around partially dissolved TiC particles (green C). The temperature achieved during LPBF allows C from TiC to diffuse and enrich Ti liquid but melt pool liquid time. The presence of remaining undissolved TiC indicates, however, that the melt pool lifetime is not sufficient to dissolve the larger fraction of the TiC particles. This is reflected by the average particle size decreasing from 9.6 µm and 37.2 µm to 6.5 µm and 9.56 µm, for TiC23 and TiC45 respectively. Similar effects were observed by Wang et al. in the LMD process, in which remaining particles sizes varied with the process parameters and the original powder size distribution [16].

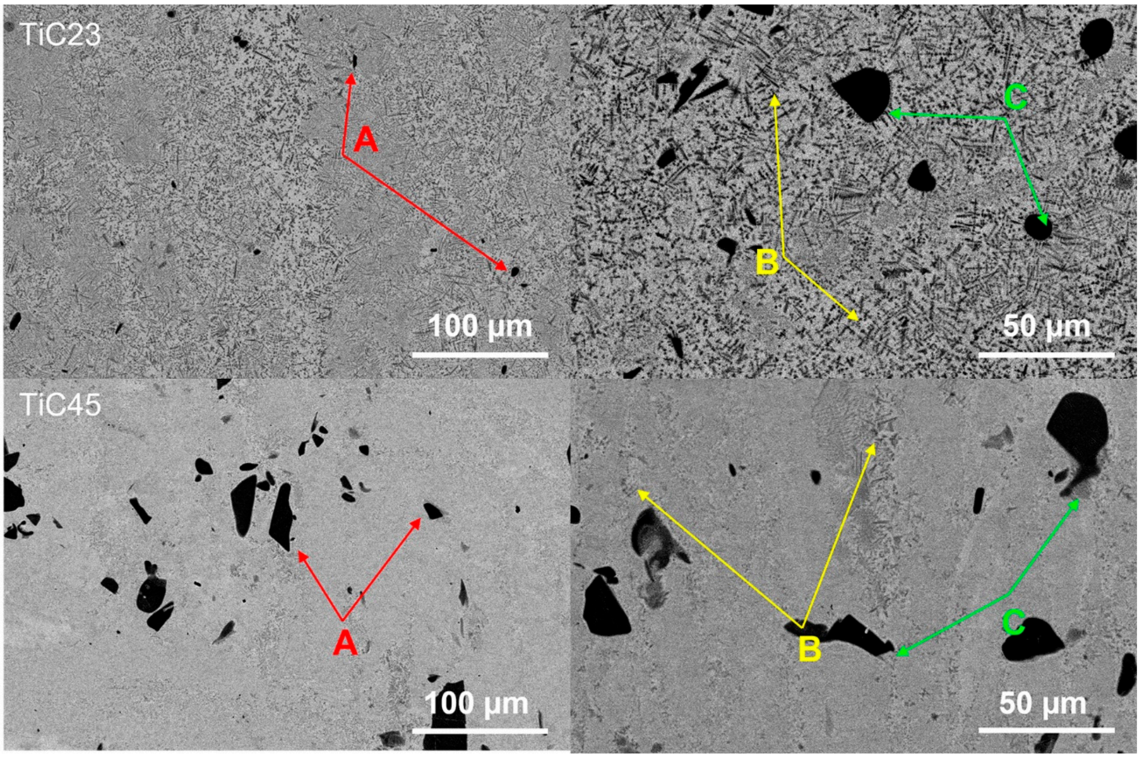

Figure 3. SEM micrographs presenting as-built microstructures for TiC23 (top) and TiC45 (bottom). Examples of un-dissolved TiC particles are indicated by the red arrows (A), primary dendritic TiC by yellow arrows (B), and secondary dendritic TiC by green arrows (C).

XRD patterns of the as-built LPBF MMC samples and feedstock powders, with selected 2-θ angles between 33° and 44°, are shown in Figure 4. Full XRD patterns as well as the 58-76° 2-θ angles regions are available in Appendix A, Figure A3 and Figure A4. The Ti powder shows a typical hexagonal α-Ti pattern. However, α-Ti and martensitic α'-Ti are rather difficult to differentiate due to close unit cells and overlapping of the reflections of α and α' phases. The rapid cooling induced in plasma-atomization would most likely lead to martensitic α'-Ti. It is also reported by Haase et al. that pure Ti produced by Laser Powder Bed Fusion has a martensitic α'-Ti microstructure [17]. Both as-built LPBF TiC23 MMC and TiC45 MMC samples display α-Ti peaks as well as TiC peaks. The latter are shifter to higher 2θ angles compared to the raw stoichiometric TiC powder (e.g. the 35.91° peak is shifted to 36.34° for TiC23 and 36.38° for TiC45). It can be explained by variation in residual stresses, by a modification of the TiC lattice constant or a combination of the two phenomena. The TiC lattice constant a_{TiC_x} is known to vary with the C/Ti ratio of TiC and was modelled empirically by Kurlov and Gusev whom fitted a second order polynomial on a large collection of literature data and obtained equation (1) [14].

$$a_{TiC_x} = 0.42055 + 0.02665x - 0.01456x^2 \pm 0.00005\ nm, \tag{1}$$

In addition, TiC peaks at 42°, 61° and 73° are split into two peaks. Rietveld refinement was used to measure the average lattice constants of α-Ti and two TiC_x phases as presented in Table 2. The lattice constant of the lower angle TiC peak subset is consistent with stoichiometric TiC particles while the lattice constant of the TiC peak subset at higher angle shift fits sub-stoichiometric TiC dendrites.

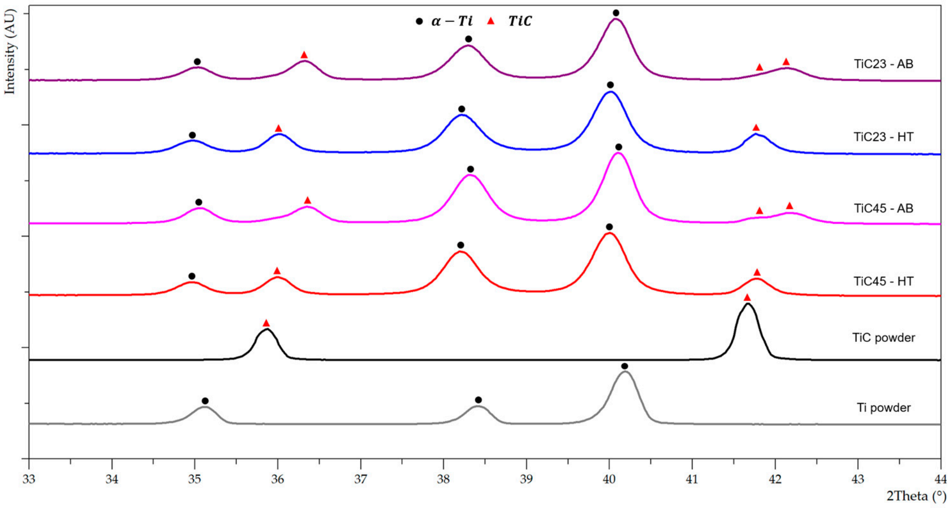

Figure 4. XRD patterns of powders feedstock, as-built LPBF TiC23 and TiC45, and heat treated LPBF TiC23 and TiC45 with 2-θ angles between 33° and 44°.

Table 2. Crystallographic parameters of TiC45 and TiC23 in as-built and heat-treated conditions. *calculated from C occupancy in TiC$_x$ [14].

Parameters	TiC45 AB	TiC23 AB	TiC45 HT	TiC23 HT
$a_{\alpha Ti}$ [Å]	2.957	2.956	2.961	2.961
$c_{\alpha Ti}$ [Å]	4.698	4.698	4.707	4.706
$c_{\alpha Ti}/a_{\alpha Ti}$ [-]	1.589	1.589	1.590	1.589
$a_{TiC_x,exp}$ [Å]	4.279	4.282	4.319	4.318
$a_{TiC_x,calc}{}^*$ [Å]	4.295	4.308	4.324	4.326
$C_{TiC_x}\ occupancy$ [-]	0.45	0.55	0.76	0.81
$a_{TiC,exp}$ [Å]	4.321	4.310	x	x
$a_{TiC,calc}{}^*$ [Å]	4.326	4.326	x	x
$C_{TiC}\ occupancy$ [-]	1.00	1.00	x	x

3.2. Heat-Treated Microstructure

Heat-treated microstructures of both TiC23 and TiC45 show a full conversion of the dendritic TiC into equiaxed TiC, while un-dissolved TiC particles do not present a significant geometrical evolution. BSE contrast between un-dissolved TiC and equiaxed TiC is softer, on average, than the contrast between un-dissolved TiC and dendritic TiC, which seems to indicate a partial homogenization of the C/Ti ratio. The diffusion process appears to be far from being completed, as there is BSE contrast within the un-dissolved TiC particles themselves. Further study of a TiC grains by STEM-EDS displays a stable C content in grains resulting from the globularisation of dendrites as presented in Figure 5. Conversely, in un-dissolved TiC grains, a decrease from the centre to the edge of the TiC grain is observed. While semi-quantitative, these results indicate that the heat treatment homogenized the C/Ti content in globularized TiC dendrites but was not sufficient to have the same effect on the un-dissolved TiC particles.

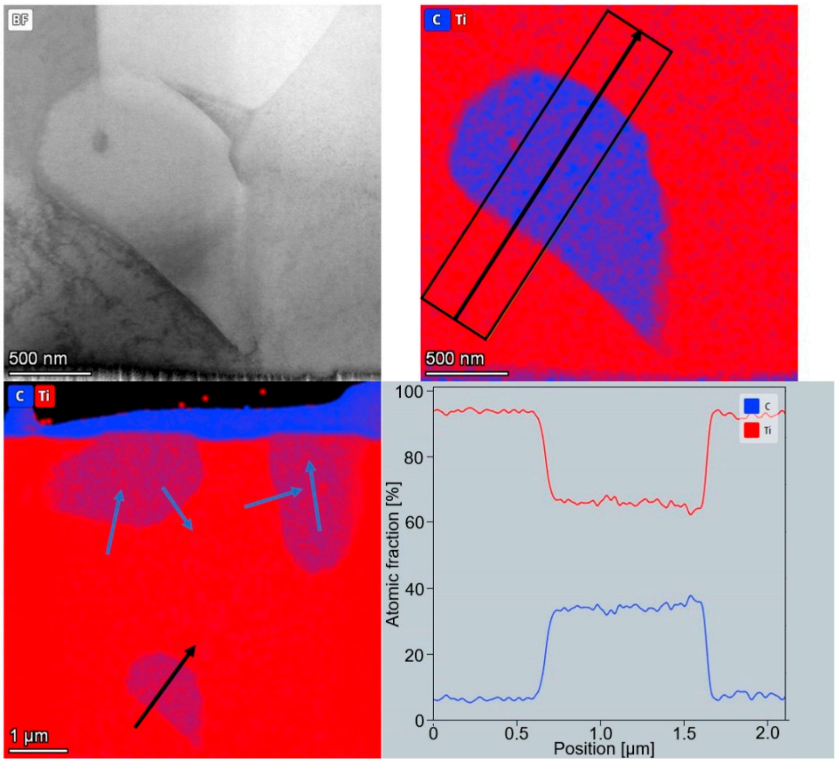

Figure 5. TEM-EDS Ti and C mapping of a TiC grain of sample TiC23 after 24h heat treatment (top-left) Bright field micrograph of a TiC grain surrounded by Ti grains. (top-right) C and Ti EDS mapping for the same region. Black arrow depicts the profile analyzed and average width used in the profile presented in (bottom-right). (bottom-left) C and Ti overlay of the TEM lamella with arrows depicting the C and Ti profiles studied. Blue arrows refer to profile not presented here.

XRD analysis after heat treatment (Figure 4) did not show significant changes in the α-Ti phase. A small uniform shift of about 0.1° is measured for all Ti peaks, which is explained by the residual stress relaxation during the heat treatment. The increase of α-Ti lattice constants after heat treatment is characterized by a constant $c_{\alpha Ti}/a_{\alpha Ti}$ ratio which is consistent with a relaxation of residual stresses and a constant C content at solubility limit (0.08 wt% at room temperature in α-Ti). Indeed, variation in the content of C in solid-solution is known to affect the $c_{\alpha Ti}/a_{\alpha Ti}$ ratio [18]. All TiC peaks shifted to lower 2-θ angles, and split peaks disappeared. The transition from split TiC peaks in as-built conditions to single TiC peaks in heat treated conditions indicates a shift from bimodal to monomodal distribution of the C content in TiC grains, i.e., heat treatment led to TiC's C/Ti ratio homogenization at sample level. The residual local variations of the C content in TiC grains observed by TEM are not resolved by XRD. The TiC peak shift is, thus, explained by a lattice change induced by the redistribution of C atoms over the TiC phases and a relaxation of the thermal residual stresses. The comparison of the experimental TiC_x lattice constant with the one calculated from C/Ti ratio using Kurlov and Gusev's relation displays a reduction of the discrepancy between experimental and calculated lattice constants after the heat treatment which is coherent with a reduction of the residual stresses of TiC [14].

High magnification micrographs of the microstructures, in Figure 7, indicate an almost full conversion of α'-Ti into α-Ti, with only a few remaining visible martensitic grains. EBSD maps at similar magnification (Figure 8) were used to statistically quantify Ti and TiC grain sizes. These analyses show that there is not a significant difference in grain size distributions between TiC23 and TiC45 (Ti grain size: 2.9±1.6 µm and 3.0±2.3 µm for TiC23 and TiC45; TiC grain size: 1.4±0.9 µm and 1.2±0.9 µm for TiC23 and TiC45). The minimal influence of the variation in feedstock properties over the microstructure dimension demonstrates tight microstructure control through the current LPBF process conditions.

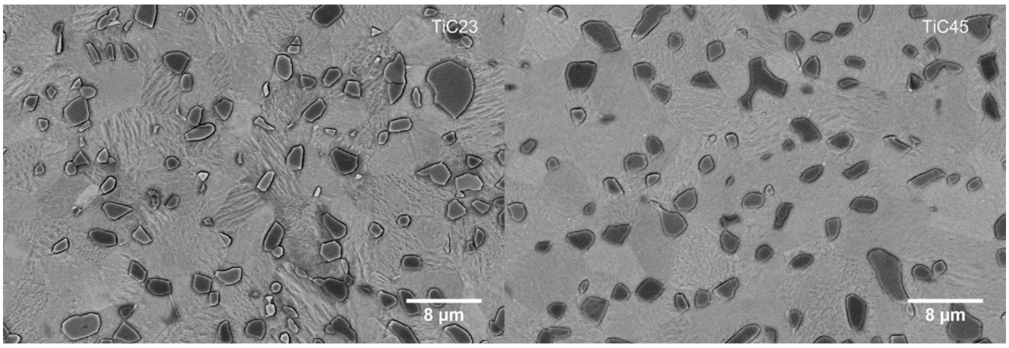

Figure 6. High magnification BSE micrograph of typical microstructure found in TiC23 (left) and TiC45 (right) heat treated samples. Grain of α-Ti phase are visible in several light grey shades thanks to grain orientation sensitivity of BSE and etching.

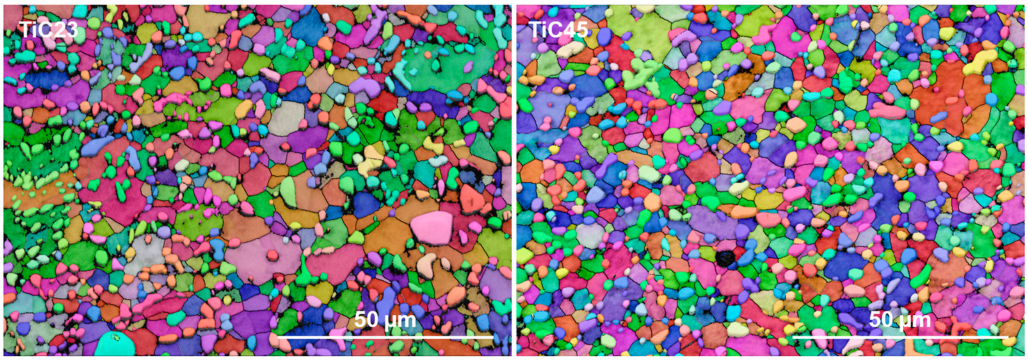

Figure 7. Typical EBSD maps of heat treated TiC23 (left) and TiC45 (right).

Generally, heat-treated microstructures had enough contrast in BSE for image analysis measurement of reinforcement content, using low magnification micrographs. The effective reinforcement content measured in TiC23 and TiC45 are 20.8±5.5 vol% and 21.5±4.7 vol% respectively, which represents almost twice the nominal value (i.e. 12 vol%). This phenomenon is explained by the reduction of the C/Ti ratio in the carbides, according to reaction (2).

$$xTiC + Ti \xrightarrow{yields} (1+x)TiC_x, \quad (2)$$

With x being the C/Ti ratio. Roger et al. showed stable C/Ti ratio of 0.57 after a 450h heat treatment at 920°C in a particulate Ti-TiC MMC with similar reinforcement content [11]. The elastic modulus was demonstrated to vary significantly as the C/Ti ratio evolve [19,21]. An empirical relation similar to the one proposed by Kurlov and Gusev for shear modulus can be fitted on the experimental data as presented in Figure 8 [14]. It led to the empirical equation (3) for the variation of the Young's modulus E_{TiC_x} with C/Ti ratio x.

$$E_{TiC_x} = 138.74 + 234.04x + 77.21x^2 \pm 16\,GPa, \quad (3)$$

Using this relation and C/Ti ratio calculated from XRD measurements, the average Young's moduli for the TiC_x phases in heat treated TiC23 and TiC45 are estimated to be 361±16 GPa and 379±16 GPa. The impact of the variation of the Young's modulus and reinforcement content with the C/Ti ratio will be discussed in a dedicated section with the experimental mechanical properties.

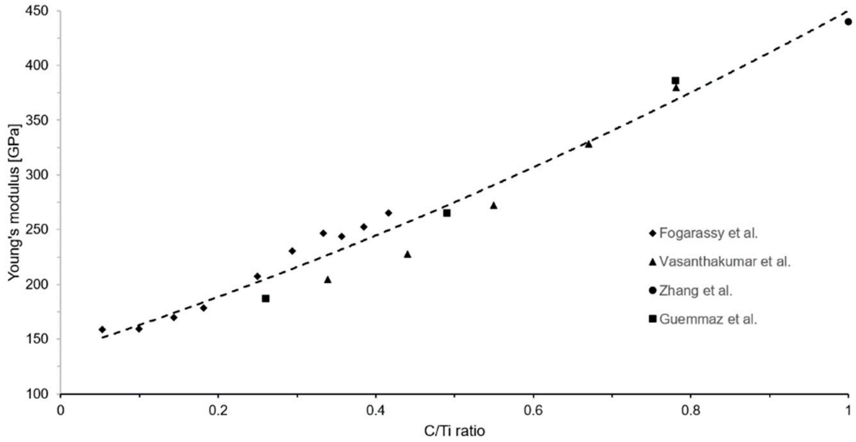

Figure 8. Young's modulus of TiC_x as a function of the C/Ti ratio. Data were fitted with a second order polynomial function resulting in equation (3) [19–22].

3.3. Density Characterization

The density was analysed globally in the sample as well as in the hatching region and contour. The porosity analysis done using image analysis of micrographs showed virtually no porosity in the hatching region, but an increased number of defects close to the edges of the samples. XCT allowed a better understanding of the spatial distribution of porosity and displayed that a majority of the porosities reside at the interface between the hatching region and the contour (Appendix A Figure A5). Hence, the "hatching density" was measured by removing all porosity outside of the hatching regions. Hatching and sample densities are compared in Table 3, indicating that the porosities outside the hatching region account for a loss of 0.3 to 0.4% density in TiC23 and TiC45, respectively. Further parameter optimization of this region could, hence, lead to a density close to 99.9% for TiC23. On the other hand, for TiC45, most of the porosity is located at other locations. One needs to note that XCT measurements had a resolution of 20 µm, which restricts this conclusion to porosities larger than this size.

Table 3. XCT density measurements. Sample density refers to the overall density of the sample. Hatching density is defined as the density of the inner region of the sample. It is calculated by removing the skin zone of the sample during the analysis.

Sample	Sample density [%]	Hatching density [%]
TiC23	99.5	99.9
TiC45	98.8	99.1

3.4. Mechanical Properties

Mechanical characterization, summarized in Table 4, shows a strong increase in Young's modulus and Ultimate Tensile Strength (UTS) in all MMCs compared to pure Ti. While as-built MMCs are brittle and do not yield, both heat treated TiC23 and TiC45 deform plastically, enough to enable the measurement of the 0.2% Yield Strength (YS) as demonstrated in Figure 9. The fracture strain is twice as large after the heat treatment and reach a similar values as reported by Yan et al. in the case of TiC45 and is 30% above it in the case of TiC23. The lower fracture strain presented by TiC45 is assumed to be due to the increase of stochastic defects density with particle size observed in ceramics. This demonstrates the effectiveness of the heat treatment used in improving the ductility of Ti-TiC MMCs. It is assumed that both the reduction of the local stress concentration (owing to the conversion of dendritic TiC to granular TiC), and the normalization of the stress field (through the homogenization of the TiC particles stoichiometry and size), leads to the ductility improvement observed. The UTS is also observed to increase after the heat treatment, while strength is, generally, known to decrease with an increase of the average grain size. In this case, the transition from brittle to relatively ductile material enables the increase in UTS. However, longer heat treatment durations are most likely to result in a decrease in strength. In heat treated MMCs, the YS was increased by 37% and 57% for TiC23 and TiC45, respectively, and the UTS by 31% and 44%. Five possible strengthening mechanisms can lead to this increase: Hall-Petch, Orowan, thermal coefficient mismatch, carbon solid-solution and load transfer. These well-known mechanisms and their distribution will not be detailed here, as strength is not the focus of this study. Stress-strain curves in Figure 9 show a stronger strain hardening for TiC 23 compared to TiC45. More experiments would be needed to define its precise origins; however, a few elements can be proposed. Larger un-dissolved particles could lead to more strain localization, as the stress plateau of TiC45 may indicate, and therefore earlier failure. Smaller particles in TiC23 would, on the other hand, increase their number and enhance dislocation-particle interactions (Orowan mechanism).

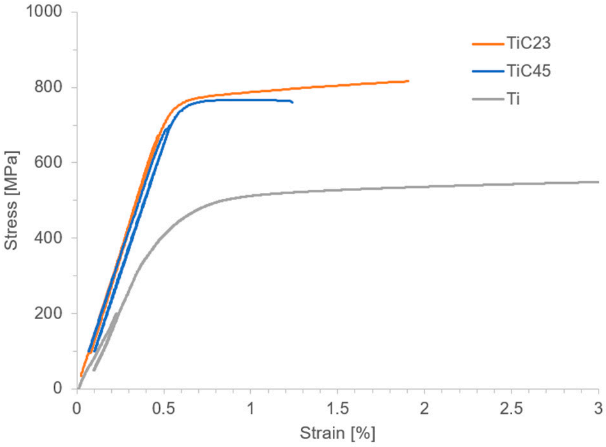

Figure 9. Stress-strain curves of typical heat-treated TiC23 and TiC45 as well as as-built Ti samples.

Table 4. Tensile properties of TiC23 and TiC45 MMC samples compared to those of the Ti reference.

	TiC45 AB	TiC45 HT	TiC23 AB	TiC23 HT	Ti
E300 [GPa]	153±4	148±7	149±17	147±4	117±7
E700 [GPa]	-	149±9	-	149±3	-
YS [MPa]	-	700±74	-	806±20	512±6
UTS [MPa]	668±21	752±11	778±15	827±9	576±4
e [%]	0.5±0.0	1.3±0.1	0.7±0.1	1.7±0.2	29.3±3.1

The Young's modulus does not appear to be affected by the heat treatment with all values slightly below 150 GPa. This elastic modulus is known to be influenced mainly by the properties of the components of the composites and their relative fraction as visible in the parameters used in standard laws of mixture such as Hashi-Shtrickman bounds [23]. In addition, in the case of elongated reinforcements, the orientation of the reinforcement can also play a significant role. However, considering the low aspect ratio of the TiC_x grains observed in heat treated conditions, this factor can be neglected in this study. The absence of significant variation of the Young's modulus during the heat treatment indicates that, on average, the variations in lattice constants, C/Ti ratios and, hence, elastic moduli, are compensated by the variation of reinforcement contents. This concept can be visualized by using Hashin-Shtrickman bounds for Ti-TiC with different TiC C/Ti ratios. The C/Ti ratio measured in TiC23 and TiC45 in heat treated condition were used, i.e., 0.81 and 0.76. The TiC Young's moduli were calculated using the empirical relation proposed in this study (3) and the Poisson ratios ν_(TiC_x) using the empirical relation (equation (4)) proposed by Kurlov and Gusev [14].

$$\nu_{TiC_x} = 0.256 - 0.0.65x \pm 0.002, \quad (4)$$

The resulting Hashin-Shtrickman bounds are presented in Figure 10 along with the Young's modulus measured for TiC23 and TiC45 in heat treated conditions. The reduction of the C/Ti ratio leads to a decrease in the expected properties. It is clearly visible in Figure 10 with the green (Ti-TiC0.81) and blue (Ti-TiC0.76) regions being lower than the grey one (Ti-TiC). The experimental values for TiC23 and TiC45 fit on the bottom bound of their relative C/Ti ratio which is coherent with the current microstructure as the lower bound is defined as a homogeneous matrix reinforced by a homogeneous distribution of spherical inclusions of reinforcement material. The definition of the higher bound is instead opposite by definition, implying that the reinforcement material contains a homogeneous distribution of spherical inclusions of matrix materials. The latter is being conceptually closer to cermets than MMCs. It is important to note that these considerations were made considering effective reinforcement content. If only nominal reinforcement was considered, experimental data would be above the higher bound of stoichiometric Ti-TiC (12 vol% and 147 GPa and 148 GPa). As introduced with expression (2), the conversion of stoichiometric TiC into TiC_x leads to an increase in the reinforcement content which cannot be neglected, e.g., in this case where effective reinforcement content is almost twice the nominal reinforcement content.

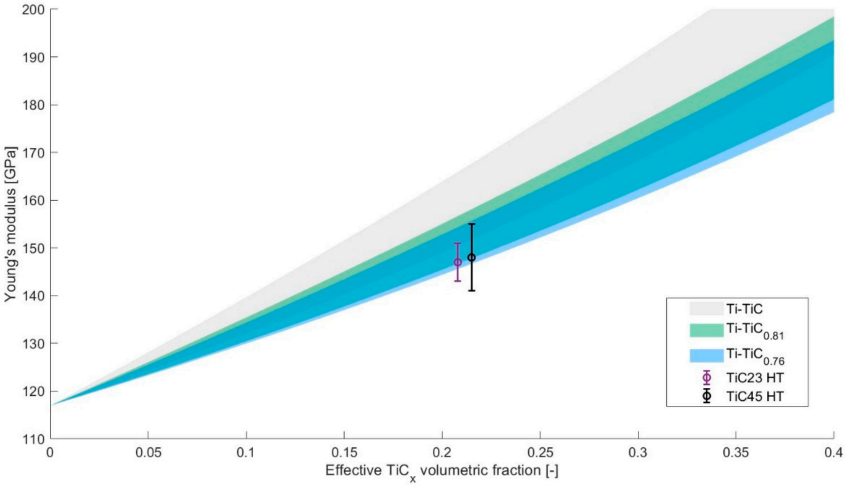

Figure 10. Young's modulus estimated by Hashin-Shtrickman bounds for Ti-TiC as a function of the TiC volumetric content [23]. Grey, green and blue regions provide the estimates for different C/Ti ratio in TiC. Experimental data from TiC23 and TiC45 in heat treated conditions are visible in purple and black, respectively.

The Young's moduli measured with the unload at 300 MPa (E300) and 700 MPa (E700) do no present significant variations which indicates the likely absence of damage or pre-existing defects in the composites. Considering the Young's moduli at the end of the process, TiC23 and TiC45 present a modulus enhancement of 26% compared to unreinforced Ti.

Fracture surface analysis, illustrated in Figure 11, showed a ductile matrix with distinctive ductile dimples together with a distribution of brittle TiC un-dissolved particles. TiC_x grains originating from the precipitated TiC dendrites were very difficult to identify on the fracture surfaces. However, cross-sections done perpendicular to the fracture surfaces did evidence their presence. Study of both fracture surfaces and sub-surface cross-sections indicates the presence of two failure mechanisms: (i) particle cracking and (ii) particle delamination. A crack can be seen progressing from one TiC_x grain to another through a deformed matrix, as well as cracked TiC_x grains and TiC un-dissolved particles close to failure points. The analysis of the full fracture surface does not show a propensity of the failure path to follow the cracked un-dissolved TiC particles. Indeed, almost none of them were found on the fracture surface of TiC23, and very few on the fracture surface of TiC45. The exact failure mechanism is however not fully understood at this point.

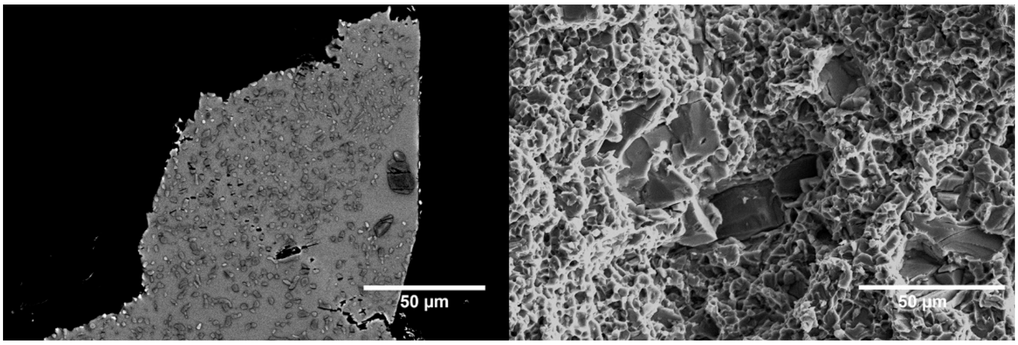

Figure 11. Fracture cross-section (left) and fracture surface (right) micrographs of a TiC23 sample after tensile failure. The fracture cross-section was extracted at the edge of the sample.

4. Conclusions

Ti-TiC MMCs with a 12 vol% reinforcement content were successfully produced using LPBF and subsequent heat treatment. Two grades of Titanium Carbide powder size distribution were used, and the microstructure and mechanical properties were thoroughly characterised and investigated.

- A density >99% was achieved with the lowest reinforcement particle sizes, while a density >98% was achieved with the other one.
- A drastic evolution of the reinforcement content (12 vol% to 21 vol%) and C/Ti ratio (0.98 to 0.8) was observed following LPBF and heat treatment. The effect of the variation of TiC elastic properties and volumetric fraction on composite elastic properties are discussed.
- Young's moduli of both MMCs were 26% higher (149 GPa) than the one of Ti.
- The fracture strain after heat treatment was more than twice the one observed in as-built conditions. The elastic modulus was not affected by the heat treatment.
- Fracture up to 1.7% were achieved after heat treatment and for lower particle size distribution. The value is 30% higher than previously reported for Ti-based MMCs produced by LPBF with similar elastic modulus.
- Lower particle sizes were shown to be beneficial for both density and mechanical properties. Further decrease of reinforcement size could lead to even higher performances.

Author Contributions: Conceptualization, Gaëtan Bernard and Vaclav Pejchal; Data curation, Gaëtan Bernard; Formal analysis, Gaëtan Bernard; Funding acquisition, Vaclav Pejchal and Olha Sereda; Investigation, Gaëtan Bernard; Methodology, Gaëtan Bernard and Vaclav Pejchal; Project administration, Vaclav Pejchal and Olha Sereda; Resources, Gaëtan Bernard; Supervision, Olha Sereda and Roland E. Logé; Validation, Gaëtan Bernard, Vaclav Pejchal and Olha Sereda; Visualization, Gaëtan Bernard; Writing – original draft, Gaëtan Bernard; Writing – review & editing, Gaëtan Bernard, Vaclav Pejchal, Olha Sereda and Roland E. Logé.

Funding: This research was partially funded by European Space Agency, grant number 4000132091/20/NL/MH/ac. Sponsor participated in the study design but was not involved in the data collection, analysis and interpretation, nor in the report writing and decision to submit a publication.

Institutional review board statement: Not applicable.

Data Availability Statement: Data will be made available on request.

Acknowledgments: G. Bernard would like to thank Dr. L. Pambaguian and Prof. M.M. Dadras as well as CSEM's 743, EPFL's LMTM and ESA's TEC-MSP groups for their technical support and recommendations.

Conflicts of Interest: The authors declare no conflicts of interest.

Appendix A

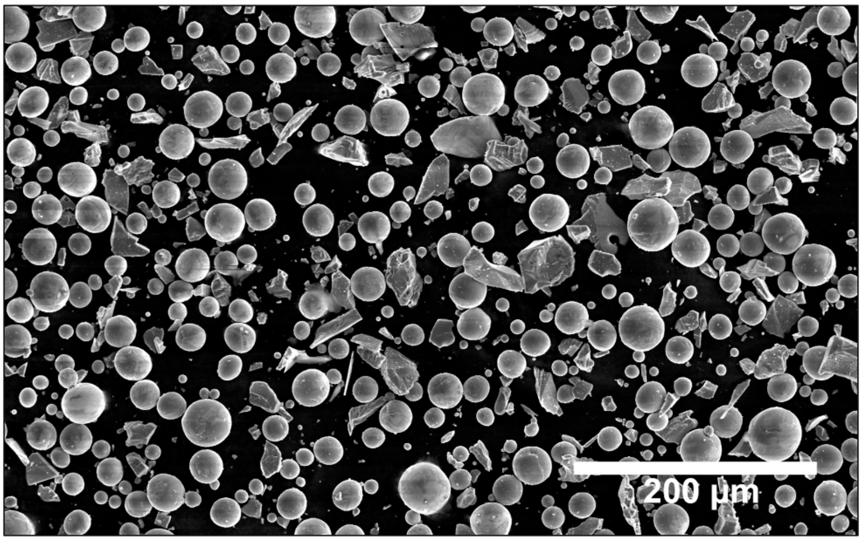

Figure A1. SEM micrograph of typical Ti-TiC powder mix.

Table A1. Dimension of the tensile sample according to ASTM E8 as well as dimension of the printed samples [15].

	ASTM E8 [mm]	Effective dimensions [mm]
G- Gauge length	10±0.1	10
D- Diameter	2.5±0.1	2.5
R- Radius of filler, min	2	2
A- Length of reduced parallel section, min	20	25

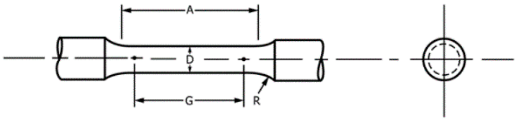

Figure A2. Geometry of the tensile samples. Figure extracted from ASTM standard E8 **Error! Reference source not found.**.

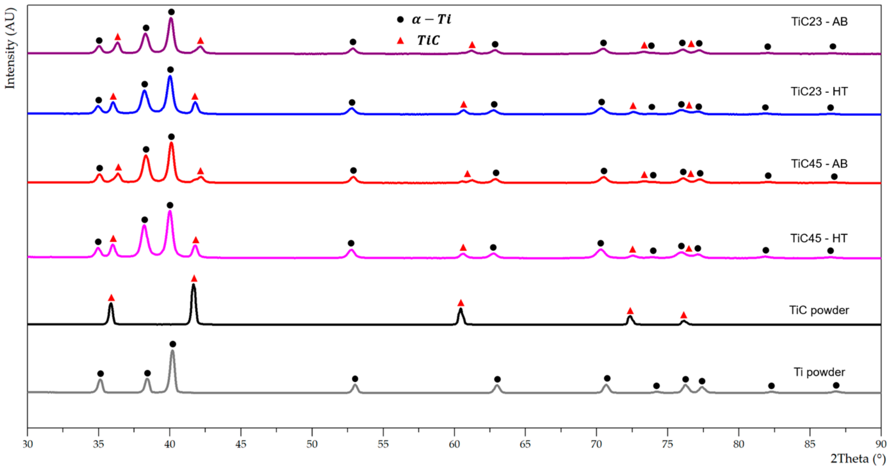

Figure A3. XRD patterns of powders feedstock, as-built LPBF TiC23 and TiC45, and heat treated LPBF TiC23 and TiC45 with 2-θ angles from 58° to 76°.

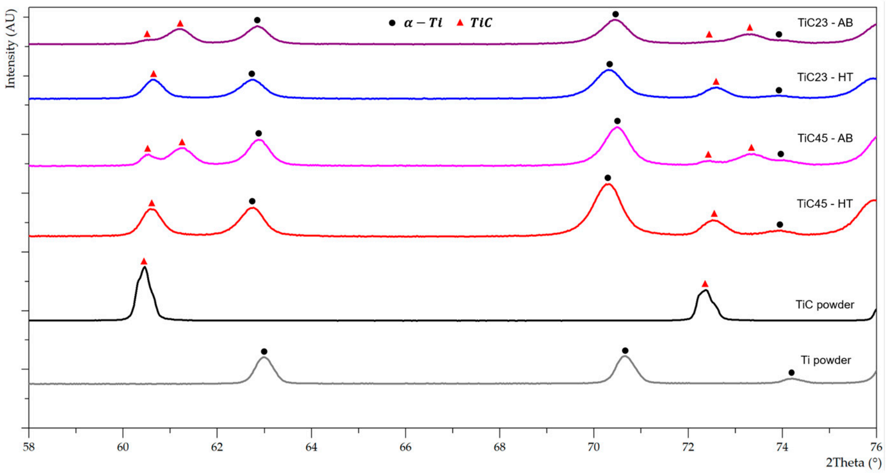

Figure A4. XRD patterns of powders feedstock, as-built LPBF TiC23 and TiC45, and heat treated LPBF TiC23 and TiC45.

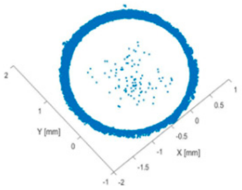

Figure A5. Integrated porosity positions over the whole reduced region of one TiC23 tensile sample.

References

1. K. S. R. Chandran, K. B. Panda, and S. S. Sahay, "TiBw-reinforced Ti composites: Processing, Properties, Application Prospects, and Research Needs" , JOM, vol. 56, no. 5, pp. 42-48, May 2004, doi: 10.1007/s11837-004-0127-1.
2. Lagos MA, Agote I, Atxaga G, Adarraga O, Pambaguian L. Fabrication and characterisation of Titanium Matrix Composites obtained using a combination of Self propagating High temperature Synthesis and Spark Plasma Sintering. Materials Science and Engineering: A Feb. 2016;655:44-49. doi: 10.1016/j.msea.2015.12.050
3. M.-K. Kim et al., "Strategies and Outlook on Metal Matrix Composites Produced Using Laser Powder Bed Fusion: A Review," Metals, vol. 13, no. 10, p. 1658, Sep. 2023, doi: 10.3390/met13101658.
4. Attar H, Ehtemam-Haghighi S, Kent D, Dargusch MS. Recent developments and opportunities in additive manufacturing of titanium-based matrix composites: A review. International Journal of Machine Tools and Manufacture Oct. 2018;133:85-102. https://doi.org/10.1016/j.ijmachtools.2018.06.003.
5. M. D. Hayat, H. Singh, Z. He, and P. Cao, "Titanium metal matrix composites: An overview," Composites Part A: Applied Science and Manufacturing, vol. 121, pp. 418–438, Jun. 2019, doi: 10.1016/j.compositesa.2019.04.005.
6. Xi L, Ding K, Gu D, Guo S, Cao M, Zhuang J, Lin K, Okulov I, Sarac B, Eckert J, Prashanth KG. Interfacial structure and wear properties of selective laser melted Ti/(TiC+TiN) composites with high content of reinforcements. Journal of Alloys and Compounds Jul. 2021;870:159436. https://doi.org/10.1016/j.jallcom.2021.159436.
7. M. Radhakrishnan, M. Hassan, B. Long, D. Otazu, T. Lienert, and O. Anderoglu, "Microstructures and properties of Ti/TiC composites fabricated by laser-directed energy deposition," Additive Manufacturing, vol. 46, p. 102198, Oct. 2021, doi: 10.1016/j.addma.2021.102198.
8. Gu D, Meng G, Li C, Meiners W, Poprawe R. Selective laser melting of TiC/Ti bulk nanocomposites: Influence of nanoscale reinforcement. Scripta Materialia Jul. 2012;67(2):185-188. https://doi.org/10.1016/j.scriptamat.2012.04.013.
9. Gu D, Hagedorn Y-C, Meiners W, Wissenbach K, Poprawe R. Nanocrystalline TiC reinforced Ti matrix bulk-form nanocomposites by Selective Laser Melting (SLM): Densification, growth mechanism and wear

behavior. Composites Science and Technology Sept. 2011;71(13):1612-1620, doi: 10.1016/j.compscitech.2011.07.010.

10. Yan Q, Chen B, Li JS. Super-high-strength graphene/titanium composites fabricated by selective laser melting. Carbon Apr. 2021;174:451 462. https://doi.org/10.1016/j.carbon.2020.12.047.
11. Andrieux J, Gardiola B, Dezellus O. Synthesis of Ti matrix composites reinforced with TiC particles: in situ synchrotron X-ray diffraction and modeling. J Mater Sci Jul. 2018;53(13):9533-9544. https://doi.org/10.1007/s10853-018-2258-8.
12. Roger J, Gardiola B, Andrieux J, Viala J-C, Dezellus O. Synthesis of Ti matrix composites reinforced with TiC particles: thermodynamic equilibrium and change in microstructure. J. Mater. Sci. Dec. 2016;13:4129-4141. https://link.springer.com/article/10.1007/s10853-016-0677-y.
13. Lin Y, Zee RH, Chin BA. In situ formation of three-dimensional TiC reinforcements in Ti-TiC composites. MTA Apr. 1991;22(4):859 865. https://doi.org/10.1007/BF02658995.
14. A. S. Kurlov and A. I. Gusev, "High-energy milling of nonstoichiometric carbides: Effect of nonstoichiometry on particle size of nanopowders," Journal of Alloys and Compounds, vol. 582, pp. 108–118, Jan. 2014, doi: 10.1016/j.jallcom.2013.08.008.
15. E28 Committee. Test Methods for Tension Testing of Metallic Materials. ASTM International. https://doi.org/10.1520/E0008_E0008M-16A.
16. Wang J, Li L, Lin P, Wang J. Effect of TiC particle size on the microstructure and tensile properties of TiCp/Ti6Al4V composites fabricated by laser melting deposition. Optics & Laser Technology Sept. 2018;105:195 206. https://doi.org/10.1016/j.optlastec.2018.03.009.
17. F. Haase, C. Siemers, and J. Rösler, "Laser powder bed fusion (LPBF) of commercially pure titanium and alloy development for the LPBF process," Front. Bioeng. Biotechnol., vol. 11, p. 1260925, Sep. 2023, doi: 10.3389/fbioe.2023.1260925.
18. A. Szkliniarz and W. Szkliniarz, "Carbon in Commercially Pure Titanium," Materials, vol. 16, no. 2, p. 711, Jan. 2023, doi: 10.3390/ma16020711.
19. Z. Fogarassy et al., "The structural and mechanical characterization of TiC and TiC/Ti thin films grown by DC magnetron sputtering," Journal of the European Ceramic Society, vol. 38, no. 7, pp. 2886–2892, Jul. 2018, doi: 10.1016/j.jeurceramsoc.2018.02.033.
20. K. Vasanthakumar and S. R. Bakshi, "Effect of C/Ti ratio on densification, microstructure and mechanical properties of TiCx prepared by reactive spark plasma sintering," Ceramics International, vol. 44, no. 1, pp. 484–494, Jan. 2018, doi: 10.1016/j.ceramint.2017.09.202.
21. M. Guemmaz, A. Mosser, L. Boudoukha, J. J. Grob, D. Raiser, and J. C. Sens, "Ion beam synthesis of non-stoichiometric titanium carbide: composition structure and nanoindentation studies," Nuclear Instruments and Methods in Physics Research Section B: Beam Interactions with Materials and Atoms, vol. 111, no. 3–4, pp. 263–270, May 1996, doi: 10.1016/0168-583X(95)01461-6.
22. J. Zhang, H. Dong, X. Li, Z. Wang, and X. Dong, "First-principles study on the stability and mechanical properties of TiCxN1-x," J Mater Sci, vol. 58, no. 10, pp. 4474–4486, Mar. 2023, doi: 10.1007/s10853-023-08144-9.
23. Hashin Z, Shtrikman S. A variational approach to the theory of the elastic behaviour of multiphase materials. Journal of the Mechanics and Physics of Solids Mar. 1963;11(2):127-140. https://doi.org/10.1016/0022-5096(63)90060-7.